

1 Vendor-neutral sequences and fully transparent workflows improve
2 inter-vendor reproducibility of quantitative MRI

3 Agah Karakuzu^{1,2*}, Labonny Biswas³, Julien Cohen-Adad^{1,4,5}, Nikola Stikov^{1,2,6}

4
5 ¹ NeuroPoly Lab, Institute of Biomedical Engineering, Polytechnique Montréal, Montréal, QC, Canada

6 ² Montréal Heart Institute, Montréal, QC, Canada

7 ³ Sunnybrook Research Institute, University of Toronto, Toronto, ON, Canada

8 ⁴ Functional Neuroimaging Unit, CRIUGM, Université de Montréal, Montréal, QC, Canada

9 ⁵ Mila - Quebec AI Institute, Montreal, QC, Canada

10 ⁶ Center for Advanced Interdisciplinary Research, Ss. Cyril and Methodius University, Skopje, North
11 Macedonia

12

13

14 **Word count:** 5701

15

16

17 * Corresponding Author: Agah Karakuzu

18 2500 Chem. De Polytechnique

19 H3T 1J4, Montreal, Quebec

20 Canada

21 Tel: +1 (514) 340-4711

22 E-mail: agah.karakuzu@polymtl.ca

23 **Abstract**

24 **Purpose:** We developed an end-to-end workflow that starts with a vendor-neutral acquisition and tested
25 the hypothesis that vendor-neutral sequences decrease inter-vendor variability of T1, MTR and MTsat
26 measurements.

27 **Methods:** We developed and deployed a vendor-neutral 3D spoiled gradient-echo (SPGR) sequence on
28 three clinical scanners by two MRI vendors. We then acquired T1 maps on the ISMRM-NIST system
29 phantom, as well as T1, MTR and MTsat maps in three healthy participants. We performed hierarchical
30 shift function analysis in vivo to characterize the differences between scanners when the vendor-neutral
31 sequence is used instead of commercial vendor implementations. Inter-vendor deviations were compared
32 for statistical significance to test the hypothesis.

33 **Results:** In the phantom, the vendor-neutral sequence reduced inter-vendor differences from 8 - 19.4%
34 to 0.2 - 5% with an overall accuracy improvement, reducing ground truth T1 deviations from 7 - 11% to
35 0.2 - 4%. In vivo we found that the variability between vendors is significantly reduced ($p = 0.015$) for
36 all maps (T1, MTR and MTsat) using the vendor-neutral sequence.

37 **Conclusion:** We conclude that vendor-neutral workflows are feasible and compatible with clinical MRI
38 scanners. The significant reduction of inter-vendor variability using vendor-neutral sequences has
39 important implications for qMRI research and for the reliability of multicenter clinical trials.

40 **Introduction**

41 As the invention of MRI approaches its 50th anniversary¹, the notion of image acquisition has almost
42 become synonymous with data collection. A major driving force in the transformation of MR images
43 from mere pictures into mineable data² is attributing physiologically relevant physical parameters to the
44 voxels, namely quantitative MRI (qMRI). MRI is not a quantitative measurement device by design.
45 Nonetheless, systematic manipulation of effective micrometer-level MRI parameters via specialized
46 acquisition methods, followed by fitting the resulting data to a signal representation or a biophysical
47 model³, can yield parametric maps, turning scanners into quantitative diagnostic tools. Despite being as
48 old as MRI itself, most of the qMRI methods have not succeeded to find widespread use in the clinic, at
49 least in part due to a major multicenter reproducibility challenge.

50 The introduction is organized around two problems hampering multicenter reproducibility of qMRI,
51 which this study seeks to address:

- 52 1. Lack of transparency and multicenter consistency in vendor implementations of pulse sequences
53 that are commonly used in qMRI
- 54 2. Technical roadblocks in the way of deploying a standardized pulse sequence along with a unified
55 user interface to multiple imaging sites

56 T1 relaxometry is a clear example of how availability, transparency and multicenter consistency of pulse
57 sequences influence multicenter reproducibility. Several methods such as inversion-recovery spin-echo
58 (IR-SE)⁴, variable flip angle (VFA-T1)⁵, Look-Locker IR⁶ and magnetization-prepared two rapid-echoes
59 (MP2RAGE)⁷ have gained popularity in MRI research. Although measured T1 values can exhibit up to
60 30% inter-sequence variability in the same scan session for the same participant⁸, a selected T1
61 relaxometry method is much more reliable within-site^{9,10}. As for the multicenter stability, MP2RAGE
62 appears to be a promising T1 mapping method at 7T with a single vendor considered¹¹. On the other
63 hand, substantial multicenter variability is reported for another popular whole-brain imaging method
64 VFA-T1, both in-vivo and in phantoms^{12,13}. Several factors contribute to the variability of the VFA-T1
65 measurement, including B1 field inhomogeneity⁸, incomplete spoiling¹⁴, sequence parameters and bore
66 temperature¹³, and uncontrolled magnetization transfer (MT) effects¹⁵. Because of all these diverse
67 confounders of T1 stability, the healthy range of in-vivo T1 values at 3T remains elusive^{16,17}. This
68 constitutes a critical problem for the potential use of T1 relaxometry in clinics.

69 Considerable amount of research has focused on the measurement bias due to acquisition-related
70 imperfections. However, the reproducibility of the developed techniques is often hindered by *problem*
71 *1*. For example, a simple yet powerful B1 correction framework for VFA-T1 has been established¹⁸, but
72 such methods are typically not available in commercial systems, or the available ones vary across
73 vendors. This not only imposes a practical challenge in evaluating the reliability of VFA-T1
74 measurements across vendors^{13,19}, but the differences between vendor-native B1 mapping methods can
75 aggravate the instability²⁰. Another example is the spoiling gradient area and RF spoiling phase
76 increment in the commercial implementations of spoiled gradient-echo (SPGR) sequences. Both
77 parameters determine the accuracy of VFA-T1 mapping. However, vendors are known to set different
78 defaults for these parameters, rendering some of them unfit for this application¹⁴. Similarly, fundamental
79 properties of the excitation pulse (e.g., pulse shape, time-bandwidth product, duration) are not disclosed
80 and it is not known how these properties are adjusted under different SAR requirements. To achieve a
81 standardized SPGR acquisition for T1 mapping, such parameter configurations should be disclosed,
82 made accessible and standardized across scanners for eliminating systematic biases. Recently, Gracien
83 et al. showed a successful example of how this solution can reduce systematic biases in relaxometry
84 mapping between two different scanner models from the same vendor²¹.

85 Addressing inadequacies of model assumptions constitutes another solution toward improving the
86 reliability of qMRI methods³. For example, balancing the total amount of RF power deposited by each
87 run of a VFA acquisition, Teixeira et al. enforced two-pool MT systems to behave like a single pool MT
88 system¹⁵. They showed that the measurement reliability increases by making the single pool assumption
89 valid through controlled saturation of MT. Although this technique holds important implications for
90 multicenter reproducibility of qMRI, deploying it to multiple sites is not a straightforward process.
91 Moreover, proprietary programming libraries of different manufacturers may not allow identical
92 implementations, exemplifying the constraints imposed by *problem 2*. Another model-related
93 improvement has been recently introduced to reduce the B1 dependency of MTsat maps by replacing the
94 fixed empirical B1 correction factor of the MT saturation-index (MTsat)²² with a correction factor map²³.
95 The proposed methodology requires the details of the saturation and excitation pulses (e.g., shape, offset,
96 duration, etc.) as the correction framework is simulation-based. From the standpoint of *problem 1*, such
97 information is not easily accessible in the stock sequence, so the correction cannot be applied. From the
98 perspective of *problem 2*, deploying sequences in multiple centers with known saturation and excitation
99 pulse parameters may not be realistic due to vendor restrictions. Even though both studies made their

100 code publicly available to facilitate the reproducibility of their work²⁴, black-box vendor strategies thwart
101 these valuable efforts.

102 Fortunately, there are several open-source pulse sequence development platforms to contend with
103 *problem 2*²⁵⁻³¹. These platforms can interpret and translate the same sequence logic for multiple vendors,
104 considerably reducing multi-center development efforts and minimizing implementation variability.
105 Another advantage of these tools is to attract community-driven development. For example, Pulseq has
106 received considerable community attention to motivate the development of sequences in Python²⁸, or
107 even going beyond code to graphically assemble³² Pulseq descriptions using Pulseq-GPI³³. Currently,
108 Pulseq can be operated on two major clinical scanners (Siemens and GE) and three pre-clinical scanner
109 platforms. There is recent literature showing the feasibility of Pulseq for performing multicenter qMRI
110 studies. For example, a standardized chemical exchange saturation (CEST) protocol has been developed
111 and deployed on three Siemens scanners, where two of the systems had different vendor software
112 versions³⁴. Results by Herz et al. showed multicenter consistency for an advanced CEST method, which
113 has been made publicly available for both Python and Matlab users. Another recent Pulseq study
114 performed inversion-recovery T1 mapping and multi-echo spin-echo T2 mapping on two Siemens
115 scanners at 1.5 and 3T in phantom³⁵. In that study the reference T1 mapping method³⁶ accurately
116 estimated T1 values within an 8% error band, whereas the T2 accuracy was slightly reduced. Taken
117 together, these studies reveal the vital role of vendor-neutral pulse sequences in standardizing qMRI
118 across centers. However, whether a vendor-neutral approach can improve quantitative agreement
119 between scanners from different vendors has remained an open question.

120 The focus of earlier open-source pulse sequence platforms was providing a rapid and unified prototyping
121 framework for facilitating interoperability, so some of the most adjusted scan parameters (e.g., field of
122 view) had to be fixed once the sequence was downloaded to the scanner. More recent solutions such as
123 GammaStar³¹ can remove this limitation by enabling user interaction through the vendor's user interface
124 to modify fundamental protocol settings during the imaging session. Offering a more complete solution
125 to *problem 2* through on-the-fly sequence updates, GammaStar eases the collaborative sequence
126 development process by providing a web-based interface. Although such technical improvements reduce
127 the barrier to entry for free sequence development, exchange and standardization, the validation aspect
128 of open-source sequences has remained elusive. Recently, Tong et al. (2021) proposed a framework for
129 testing, documenting and sharing open-source pulse sequences³⁵, which adds an important missing piece
130 to the community-driven MRI development puzzle.

131 RTHawk³⁷ is another vendor-neutral solution, which is a proprietary platform for MRI software
132 development. As it is utilizing the same infrastructure as an FDA approved (510(k), No: K1833274)
133 cardiac imaging platform, it ensures operation within MRI hardware and safety limits. Unlike the above-
134 mentioned solutions, RTHawk provides a remote procedure call (RPC) server that replaces the vendor's
135 pulse sequence controller to orchestrate vendor-specific low-level hardware instructions. The RPC pulse
136 sequence server receives control commands and relevant sequence components (i.e., RF and gradient
137 waveforms, ADC and timing events designed in SpinBench, as shown in Fig. 1c) directly from a
138 standalone Ubuntu workstation connected to the scanner network (Fig. 1a). This gives the flexibility to
139 issue synchronous or asynchronous updates to a sequence in real-time, such as scaling/replacing
140 waveforms between TRs or changing the volume prescription. As the sequence control manager is
141 decoupled from the vendor's workstation, RTHawk makes it possible to develop a vendor-neutral
142 unified user interface (UUI) per application (Fig. 1b). In addition, the collected raw data is streamed
143 over to the standalone Ubuntu workstation through a real-time transport protocol (RTP). The RTP data
144 manager enables adding or changing the metadata associated with each observation, which enables
145 exporting raw and reconstructed images in community data standards (Fig. 1d).

146 Aside from vendor-neutral experiments, researchers looked at improving qMRI stability by customizing
147 vendor-native implementations and equalizing parameters to the utmost extent possible^{21,38,39}.
148 Nevertheless, downstream data harmonization methods were still needed to correct for certain inter-
149 vendor differences³⁹, or some of the bias could not be removed altogether³⁸. This is because vendor-
150 native sequence customization may not offer a standard qMRI protocol, even for scanners with
151 comparable hardware specs, as the selection of sequence design elements is exclusive to each
152 manufacturer.

153 In this study, we test the hypothesis that vendor-neutral sequences reduce inter-vendor variability of T1,
154 MTR and MTsat measurements. To test this hypothesis, we developed an end-to-end solution starting
155 with a pulse sequence developed on RTHawk, followed by a fully transparent qMRLab workflow. We
156 compared vendor-native T1, MTR and MTsat maps⁴⁰ with those obtained using the developed vendor-
157 neutral sequence (VENUS) workflow in three healthy participants, across three different scanners
158 models from two manufacturers at 3T.

159 **Methods**

160 *Vendor-neutral pulse sequence development*

161 We deployed vendor-neutral pulse sequences developed in RTHawk v3.0.0 (rc4-28-ge3540dda19)
162 (HeartVista Inc., CA, USA) on three 3T systems: (G1) GE Discovery 750 software version DV25
163 (R02_1549.b) (GE Healthcare, Milwaukee, MI, USA), (S1) Siemens Prisma software version
164 VE11C (N4_LATEST_20160120) (Siemens Healthineers, Erlangen, Germany) and (S2) Siemens
165 Skyra with the same software version as (ii). Throughout the rest of this article, these scanners will
166 be referred to as G1, S1 and S2, respectively. Fig.-1a illustrates the hardware and software
167 components of the experimental setup.

168 *General design considerations*

169 All vendor-neutral protocols were based on a 3D SPGR pulse sequence⁴¹, with the RF, gradient
170 waveforms, and the readout scheme developed as independent sequence blocks in SpinBench-
171 v2.5.2 (Fig. 1c). To modify these sequence blocks, an RTHawk application and an additional UI
172 were developed for quantitative imaging, allowing the user to manage relevant acquisition
173 parameters (e.g., FA, TR, and MT pulse for MTsat) from one simple panel that is vendor-neutral
174 (Fig. 1b). Identical scan geometry and pre-acquisition settings were transferred between each
175 individual acquisition. To avoid signal clipping, the highest SNR acquisition (i.e., T1w acquisition
176 of the MTsat protocol) were run first. A simple sum-of-squares multi-coil reconstruction was
177 developed with a Fermi filter (transition width = 0.01, radius = 0.48, both expressed as a proportion
178 of the FOV) (Fig. 1d).

179 All the metadata annotations, accumulation logic of the collected data and naming of the exported
180 images were designed according to the community data standards: ISMRM-RD⁴² for the k-space
181 data and the Brain Imaging Data Structure (BIDS) for the reconstructed images^{43,44}.

182 *The vendor-neutral protocol*

183 A slab-selective (thickness = 50mm, gradient net area = 4.24 cyc/thickness) SINC excitation pulse
184 (time-bandwidth product ($T\Delta f$) = 8, duration = 1.03ms, Hanning windowed) was implemented
185 with a quadratic phase increment of 117° for RF spoiling. This was followed by a fully-sampled
186 3D cartesian readout. The default geometry properties were 256x256 acquisition matrix, 25.6 cm

187 FOV and 20 partitions in the slab-selection direction, yielding 1x1x3 mm resolution. The readout
188 gradient had a rewriter lobe with 2 cyc/pixel net area and was followed by a spoiling gradient
189 with an area of 40 mT·ms/m.

190 For the magnetization transfer (MT) saturation, a Fermi pulse (duration = 12ms, $B_{1rms} = 3.64\mu T$,
191 frequency offset = 1.2kHz, transition width = 0.35, max $B_1 = 5\mu T$, pulse angle = 490°) was
192 designed as an optional block. A loop command was defined for the sequence to iterate through
193 three sets of parameters (i.e., MT, FA and TR), defined by the user in the UI for a complete
194 MTsat protocol.

195 From this protocol we acquired three images: (i) PD-weighted SPGR with no MT, FA = 6° and
196 TR = 32ms (ii) MT-weighted SPGR with MT, FA = 6° and TR = 32ms (iii) T1-weighted SPGR
197 without MT, FA = 20° and TR = 18ms. From images (i) and (iii) we computed a T1 map, from
198 images (i) and (ii) we computed an MTR map, and from images (i), (ii) and (iii) we computed an
199 MTsat map.

200 *Data acquisition*

201 Three healthy male participants volunteered for multi-center data collection. Written informed
202 consent was acquired prior to the data collection following a protocol approved by the Ethics
203 Committee of each imaging center.

204 The participants (P1-3) and the ISMRM-NIST system phantom (HPD Inc., serial number = 42)
205 were scanned on three imaging systems at two imaging sites. In S1 and S2, the phantom was
206 scanned using a 20-channel head coil due to space constraints, whereas a 32-channel coil was used
207 in G1. For in-vivo imaging, 32-channel head coils were used in G1 and S1, whereas a 64-channel
208 coil was used in S2. S1 was equipped with an XR-K2309_2250V_951A (Siemens Healthineers,
209 Erlangen,Germany) gradient system (80 mT/m maximum amplitude and 200 T/m/s slew rate per
210 axis, 50 cm maximum FOV), S2 with an XQ-K2309_2250V_793A (Siemens Healthineers,
211 Erlangen,Germany) gradient system (45 mT/m maximum amplitude and 200 T/m/s slew rate per
212 axis, 50 cm maximum FOV) and G1 with a 8920-XGD (GE Healthcare, Milwaukee, USA)
213 gradient system (50 mT/m maximum amplitude and 200 T/m/s slew rate per axis, 48cm maximum
214 FOV). The nominal field strengths on G1 and S1-2 were 3T and 2.89T, respectively. Before the
215 scan, the phantom was kept in the imaging site for at least a day, and in the scanner room for at

216 least 3 hours. The measured bore temperature in G1, S1 and S2 was 20.1°C, 20.2°C and 20.8°C,
217 respectively.

218 The acquisition parameters were set according to a generic protocol established for MTsat imaging
219 of neural tissue⁴⁵. The vendor-neutral acquisition parameters were identical on all systems.
220 However, it was not possible to equalize all the parameters between the vendor-native protocols.
221 Comparison of vendor-native and vendor-neutral protocols are presented in Table 1. To scan the
222 phantom, prescan measurements were performed as described by Keenan et al. (2021) and the
223 vendor-neutral acquisitions were configured to start the acquisitions with these calibrations¹³. For
224 all acquisitions, the prescan settings of the initial T1w acquisition were used for the subsequent
225 PDw and MTw acquisitions on all vendor systems. For the VENUS acquisitions, B0 shimming
226 gradients were set using a spiral multi-echo gradient-echo sequence. Gradient non-linearity
227 correction was performed as part of the on-site reconstruction pipeline. The warping coefficients
228 were made available for offline reconstruction. For the systems S1-2, the identical protocol was
229 used by exporting the vendor-native protocol files from S2. The protocols for G1 were set on-site.

230 *Data processing*

231 All the processing was performed using data-driven and container mediated pipelines comprised
232 of two docker images (Fig. 2). Quantitative fitting was performed in qMRLab⁴⁶ v2.5.0b. Pre-
233 processing steps were performed using ANTs⁴⁷ for registration and FSL⁴⁸ for automatic gray-
234 matter (GM) and white-matter (WM) segmentation.

235 For the in-vivo data, between-scan motion correction was performed by aligning PDw and MTw
236 images onto the T1w, followed by MTsat fitting (Fig. 2b). Brain region segmentations were
237 performed on the T1w images and ROI masking was performed to prepare data for statistical
238 analyses (Fig. 2c). The phantom T1 pipeline consisted of linearized VFA-T1 by accounting for
239 varying TRs²² (Fig. 2a). Resultant phantom maps were then masked using spherical ROIs as
240 described in⁴⁹. Finally, peak SNR (PSNR) values were calculated, and the phantom images were
241 visualized to compare image quality characteristics between vendor-native and VENUS
242 implementations (Fig. 3).

243 *Statistical analyses*

244 All the descriptive statistics were reported by the processing pipeline in tabular format for phantom
245 and in-vivo maps (available at <https://osf.io/5n3cu>). Vendor-neutral and vendor-native phantom

246 measurement performances were compared against the reference (Fig. 4b,c) and percent deviations
247 from the ground truth were reported (Fig. 4d).

248 Kernel density estimates of the T1, MTR and MTsat distributions in WM and GM were visualized
249 as ridgeline plots for one participant (Fig. 5d-i). Before the statistical comparisons in WM, the
250 outliers were removed from the distributions. The non-outlier range was 0 to 3s for T1, 35 to 70%
251 for MTR and 1 to 8 for MTsat. Filtered distributions were then randomly sampled to obtain an
252 equal number of WM voxels ($N = 37,000$) for a balanced comparison.

253 Percentile bootstrap based shift function analysis⁵⁰ was performed to compare dependent
254 measurements of T1, MTR and MTsat in WM ($N=37,000$) between different systems (G1-vs-S1,
255 G1-vs-S2 and S1-vs-S2) for VENUS and for the vendor-native implementations. Deciles of the
256 distributions were computed using a Harrell-Davis quantile estimator⁵¹. The decile differences
257 were calculated using 250 bootstrap samples to characterize differences at any location of the
258 distributions (Fig. 6a). For convenience, we annotated the 5th decile (median) with the respective
259 percent difference (Fig. 6b-d). To characterize the difference between scanners across the
260 participants, the shift function was extended to a hierarchical design (Fig. 7a). Similarly, percent
261 T1, MTR and MTsat differences between scanners at the median deciles were annotated per
262 subject, and the average percent deviations were reported (Fig. 7b-d). The reader is welcome to
263 reproduce these figures online, where necessary changes can be made to visualize the high-density
264 intervals of the decile differences at <https://github.com/qMRLab/VENUS>.

265 Finally, quantitative measurement discrepancies of vendor-native and VENUS implementations
266 between different vendors were compared using Wilcoxon signed rank test. The comparison was
267 performed on the G1-vs-S1 and G1-vs-S2 percent absolute differences of T1, MTR and MTsat in
268 white matter between vendor-native and vendor-neutral implementations. The level of significance
269 was set at $p = 0.05$.

270 Results

271 The contrast characteristics of VENUS and vendor-native T1w phantom images are qualitatively
272 comparable (Fig. 3h-m). In addition, VENUS PSNR values are on a par with those of vendor-
273 native T1w and PDw images (Fig. 3a). The resolution markers are discernible in the vendor-neutral
274 images (Fig. 3b-d) with a slightly lower horizontal resolution compared to the S1-2_{NATIVE} (Fig.
275 3f,g). On the other hand, the insert pattern resolution of G1_{NATIVE} (Fig. 3e) appears lower than that
276 of G1_{VENUS} (Fig. 3b).

277 Overall, the vendor-neutral implementation reduces inter-vendor variability and brings T1
278 estimations closer to the ground truth of the phantom, particularly for the targeted physiological
279 interval from 0.7 to 1.9s (Fig. 4b). On the other hand, T1 deviations ($\Delta T1$) calculated by percent
280 error indicate that G1_{NATIVE} and S2_{NATIVE} exhibit a persistent overestimation trend, with S1_{NATIVE}
281 showing a relatively better accuracy (Fig. 4c). Within the same interval, the highest deviation is
282 observed for G1_{NATIVE}, where $\Delta T1$ ranges from 9.7 to 30.4%. For R4-6, G1_{NATIVE} and G1_{VENUS} T1
283 measurements straddle the reference, where G1_{VENUS} shows 5.1-13.8% underestimation and the
284 G1_{NATIVE} overestimation remains within the 3.4-10.5% interval (Fig. 4c). For lower T1 reference
285 values ($T1 < 170\text{ms}$), all measurements indicate higher deviations, with S1-2_{NATIVE} performing
286 better than S1-2_{VENUS}.

287 When the measured T1 values are averaged over S1-2 (\bar{S}), the differences between G1_{NATIVE} and
288 \bar{S}_{NATIVE} are 8, 11, 12.5 and 19.4%, whereas the differences between G1_{VENUS} and \bar{S}_{VENUS} are 5, 2,
289 2 and 0.2% for R7-10, respectively (Fig. 4d). This reduction in between-vendor differences
290 brought by VENUS is coupled with an improvement in accuracy. When averaged according to the
291 implementation type, average VENUS deviation ($\overline{\Delta T1}_{\text{VENUS}}$) falls within the 0.2 - 4% range and
292 $\overline{\Delta T1}_{\text{NATIVE}}$ ranges from 7 to 11%. Even though G1_{NATIVE} has the dominant contribution to the
293 higher $\overline{\Delta T1}_{\text{NATIVE}}$ values, Fig. 4d shows that \bar{S}_{VENUS} is closer to the reference than \bar{S}_{NATIVE} for most
294 of the R7-10 ($\Delta T1$ of 7.6, 3.5, 5.4, 0.7% and 3.2, 0.9, 2, 1.3% for \bar{S}_{NATIVE} and \bar{S}_{VENUS} , respectively).
295 As a result, VENUS reduces between-vendor differences with an overall accuracy improvement.

296 Figure 5 shows in vivo T1, MTR and MTsat maps from a single participant (P3). While most of
297 the improvements are evident from the maps (5a - 5c), the ridgeline plots (5d - 5i) make it easier
298 to appreciate the VENUS vs vendor-native distribution differences in the GM and WM per metric.

299 Consistent with the higher myelin content in WM, T1 values are lower in WM (around $1.1 \pm 0.2s$,
300 Fig. 5d), whereas MTR and MTsat values are higher (around $50 \pm 8\%$ and 3.8 ± 0.9 a.u., Fig. 5
301 e,f) in comparison to those in GM ($1.9 \pm 0.4s$, $40 \pm 2\%$ and 1.8 ± 0.5 , for T1, MTR and MTsat,
302 respectively, Fig. 5g-i). The general trend observed in the images is captured by ridgeline plots,
303 showing better agreement between VENUS distributions of G1, S1 and S2. This is further
304 supported by the between-scanner coefficient of variation (CoV) per metric (Table 2), showing
305 that VENUS reduces the CoV from 16.5, 10.1 and 12.5% to 6.1, 4.1 and 4.1% for T1, MTR and
306 MTsat, respectively. This indicates a sizable decrease in between-scanner variability using
307 VENUS compared with vendor-native measurements and the trend is consistent across
308 participants.

309 Going from vendor-native (top rows, blue panels) to VENUS (bottom rows, red panels), Fig. 6b-
310 d indicates a decrease in T1, MTR and MTsat WM differences between scanners from different
311 vendors (G1-vs-S1 and G1-vs-S2) for P3, without exception and throughout the deciles. One can
312 also appreciate the changes in shift function shapes. For example, the shift function for G1_{NATIVE}
313 vs S2_{NATIVE} MTsat comparison in Fig. 6d shows a positive linear trend, indicating that WM voxels
314 with higher MTsat values tend to show a higher between-vendor difference. On the other hand,
315 the G1_{VENUS} vs S2_{VENUS} MTsat shift function appears flatter, describing a more uniform (and
316 reduced) bias throughout the WM distribution. As for within-vendor comparisons (S1-vs-S2) of
317 the same participant, VENUS reduces difference scores for T1 and MTsat by 5.8 and 7.8% while
318 increasing that for MTR by 5.3% (Fig. 6).

319 Figure 7 expands on Figure 6 for multiple participants by overlaying individual shift functions
320 (shades of pink) and illustrating the across-participants trend using group shift functions that are
321 red for VENUS and blue for vendor-native differences (Fig. 7a). Overall, VENUS G1-vs-S1 and
322 G1-vs-S2 differences are on the order of 2.3 to 7.9%, whereas the vendor-native variations start
323 from 13.8% and extends up to 25.6%, averaged across participants. The reduction in between-
324 vendor differences achieved by VENUS is significant after correction for multiple comparisons
325 for all maps ($p=0.015$). Another general observation is that individual shift function shapes are
326 mostly consistent across participants, indicating that the inter-scanner differences between the
327 VENUS and vendor-native implementations are not modified by anatomical differences. However,
328 the magnitude of the difference is participant-specific. For example, P3 shows the highest
329 G1_{NATIVE} vs S1_{NATIVE} T1 difference of 31.2%, which is followed by 20.9 and 14.2% for P2 and P1,

330 respectively (Fig. 7b). Finally, within-vendor effect of VENUS remains on the lower side with all
331 participants considered, reducing the S1-vs-S2 difference by 3.2 and 2.0% for T1 and MTsat while
332 increasing that for MTR by 3.7%.

333 **Discussion**

334 In this study, we developed and deployed a vendor-neutral qMRI protocol (VENUS) for T1, MTR
335 and MTsat mapping on three 3T commercial scanners by two vendors. Our findings confirm the
336 hypothesis that vendor-neutral sequences decrease inter-vendor variability of T1, MTR and MTsat
337 measurements. This key improvement addresses *problem 1*, as stated in the Introduction, with
338 open-source pulse sequence descriptions. The developed sequence can be run on most GE and
339 Siemens scanners through RTHawk software and an additional UUI that allows users to prescribe
340 customized file naming entities for exporting reconstructed images in the BIDS^{43,44} and k-space
341 data in the ISMRM-RD format⁴². Conforming with community data standards, providing a user-
342 friendly solution with a simplified vendor-neutral deployment, this work offers a complete solution
343 for *problem 2*, and shows a way forward for the standardization of qMRI.

344 *Developing an end-to-end qMRI workflow*

345 First, we created a vendor-native qMRI protocol that is unified across vendors to the greatest extent
346 possible, by keeping contrast, timing, and acquisition geometry identical (Table 1). However, other
347 vendor-native implementation details such as RF spoiling, MT and excitation pulse characteristics
348 were different, as it is commonly the case in multicenter studies^{14,38}. Trying to address these issues
349 is difficult with a vendor-native sequence given that the implementations of commercial stock
350 sequences commonly used for qMRI are not open (*problem 1*). One candidate solution for this
351 problem is modifying sequences on the vendor's proprietary development environment to equalize
352 implementations as much as possible, which has been shown to improve reproducibility to some
353 extent²¹. However, this requires familiarity with multiple sequence development environments and
354 still may fall short in unifying all the aspects on-site. Not only is this approach impractical for the
355 developers, but it is also not a user-friendly solution for clinical use. As we mention in the context
356 of *problem 2*, reproducibility solutions unifying inter-vendor implementations become more
357 favorable if they are designed with clinicians' needs in mind. To that end, we aimed at providing
358 a unified and smooth user experience by developing VENUS as an RTHawk application, which
359 allows implementation details to be shared publicly starting at the pulse sequence level.

360 Second, we built from scratch a vendor-neutral sequence that was developed and tested on a single
361 site and then ported to two more scanners from different vendors. In doing so, we adapted a system
362 that is primarily geared toward real-time imaging (RTHawk) to perform quantitative MRI
363 measurements. For example, absolute gradient limits have been allowed to achieve higher spoiling
364 gradient moments and string-valued customized metadata injection has been enabled to follow
365 community data standards⁴²⁻⁴⁴.

366 Third, we created a fully transparent, container-mediated and data-driven workflow^{52,53} that
367 automates the processing and reduces variability introduced by the operators. By design, the
368 workflow operates according to the BIDS qMRI standard⁴⁴ for picking up all the necessary data
369 and metadata, and generates outputs following a consistent derivative hierarchy. Moreover, the
370 raw data is exported in the ISMRM-RD format by our vendor-neutral sequence, allowing the use
371 of community developed reconstruction tools by simply adding another container at the beginning
372 of our modular workflow. We envision that using open-source reconstruction tools would be
373 highly favourable for vendor-neutral sequences employing under-sampled k-space with complex
374 trajectories to guarantee reproducibility⁵⁴⁻⁵⁷.

375 ***Reducing inter-vendor variability***

376 Stock sequences are optimized for reliable clinical imaging. These optimizations do not necessarily
377 serve for accuracy when the sequences are used for qMRI experiments. For example, the phase
378 increment values of S1-2_{NATIVE} sequences (Table 1) are hardcoded to maximize in-vivo signal
379 stability⁵⁸, not T1 accuracy in phantoms⁵⁹. On the other hand, the phase increment of G1 has been
380 shown to be unsuitable for T1 mapping, exhibiting severe overestimations¹⁴. In this study, we set
381 the value (117°) suggested for T1 accuracy¹⁴ while unifying all other aspects of the vendor-neutral
382 acquisition between scanners. The results from the phantom analysis clearly demonstrate that
383 VENUS achieves higher accuracy and a notable reduction in inter-vendor variability compared to
384 its vendor-native counterparts (Fig. 4).

385 In the absence of an in-vivo ground-truth T1 map (from inversion recovery), we only looked at the
386 agreement between the three implementations and explored whether VENUS brought the T1
387 values closer across vendors when compared to the vendor-native sequences. Visually (Fig. 5a),
388 the reduction in T1 variability can be appreciated for VENUS within the dynamic range of T1
389 adjusted for WM/GM. As supported by the ridgeline plots (Fig. 5d,g), the G1_{NATIVE} T1 distribution

390 is globally shifted towards higher values compared to S1-2_{NATIVE}, and their central tendency
391 differs. As observed in the phantom, G1_{VENUS} alleviates this discrepancy, shifting the T1
392 distribution closer to those of S1-2_{VENUS}. Interestingly, the WM T1 distributions appear more
393 unimodal on G1 compared to S1-2 (both for VENUS and vendor-native), with a more pronounced
394 bimodal appearance for S1-2_{VENUS}. A plausible explanation for that are vendor and implementation
395 specific differences due to B1+ field inhomogeneity. Nevertheless, the VENUS shift functions for
396 G1-vs-S1 and G1-vs-S2 comparisons are flatter than the vendor-native shift functions (Fig. 6b),
397 indicating that the inter-vendor WM T1 statistical distribution characteristics are more similar
398 using VENUS.

399 Table 2 indicates that reduction in inter-vendor variability is not limited to T1 but persists for all
400 the metrics across all participants. The inter-vendor variability in MTR and MTsat is relatively
401 easier to appreciate visually (Fig. 5b,c). The three MTR and MTsat maps from VENUS are in
402 better agreement, and this is most likely because our unified implementation compensated for the
403 MT saturation pulse differences (Table 1).

404 Reducing variability matters as much as which tools we use to assess it. Shift functions⁵⁰ take the
405 comparison beyond differences in point estimates of centrality and relative spread (CoV) to a
406 robust characterization of differences on the absolute scale of the measurement. This makes the
407 shift function analysis (Fig. 6-7) more informative than CoV (Table 2) by characterizing how
408 distributions differ for P3. For example, Table 2 shows that VENUS reduces CoV from 12.1 to
409 4.1% for MTsat. Figure 6d explains that most of that reduction is achieved by decreasing the
410 absolute G1-vs-S2 MTsat difference from 1.1 to 0.1 (a.u.), corresponding to a reduction of the
411 inter-vendor difference from 25.7% to 3.2%. In addition, Fig. 6d indicates that higher deciles
412 benefit from the G1-vs-S2 variability reduction more compared to the lower deciles, yielding a
413 flatter shift function for VENUS. This suggests that VENUS not only brings averaged MTsat
414 values closer, but also matches their distribution shape (Fig. 5f).

415 ***Implications of vendor-neutrality and the importance of transparency***

416 The most important contribution of this article is the vendor-neutral solution it provides for multi-
417 center qMRI by significantly reducing inter-vendor variability. This issue has been hampering the
418 standardization of qMRI methods for multi-center clinical trials⁶⁰, validation^{61,62}, establishing
419 protocols¹⁷, applied neuroimaging studies⁶³, determining the range of parameters in pathology^{64,65}

420 and in health^{16,38}, scanner upgrades⁴⁹ and even for phantom studies^{12,13}. By reducing such
421 variabilities, the VENUS approach can bring qMRI closer to teasing out the true biological
422 variability in quantifying in-vivo tissue microstructure⁶⁶.

423 We recognize that part of the RTHawk workflow is proprietary. Hence, we emphasize the
424 importance of the transparency to inter-vendor reproducibility at the level of sequence definitions.
425 RTHawk allows sharing open-source sequences (https://github.com/qMRLab/mt_sat). Note that
426 neither RTHawk nor open-source solutions can access under the hood of vendor-specific drivers
427 to guarantee that open-source sequences are executed according to the published code. To achieve
428 such open-execution⁶⁷, vendor-neutral solutions should be coupled with open-hardware⁶⁸.
429 Although RTHawk's pulse sequence and data management servers give more flexibility to the
430 scanner operation at multiple levels of the workflow (e.g., UUI, customized raw data stream,
431 asynchronous real-time updates to sequences, standalone workstation etc.), the conversion of the
432 open-source sequence descriptions to vendor-specific hardware instructions is not transparent. We
433 argue that this is a reasonable trade-off as it peels another layer from a vendor-specific ecosystem,
434 and it does not sacrifice the transparency of sources relevant to a pulse sequence description. The
435 accuracy and reliability of the parameter estimation depend on these descriptions; therefore, for
436 qMRI to work we need to be able to access, modify, and share the methods⁶⁹. Fortunately, the
437 VENUS approach to qMRI is not framework-exclusive and satisfies this key requirement.

438 Namely, using community developed tools such as Pulseseq, GammaStar, SequenceTree, ODIN or
439 TOPPE, interoperable qMRI applications can be developed. A critical step to achieve this is
440 effective communication between method developers to foster compatibility between frameworks.
441 This is nicely exemplified by GammaStar and JEMRIS, as both applications can export Pulseseq
442 descriptions. Enabling a similar feature by developing a SpinBench plugin is among our future
443 goals. To facilitate discussions on this topic with vendor-neutral framework developers, we created
444 a forum page on the code repository of this article (<https://github.com/qMRLab/VENUS>).

445 *Limitations and future directions*

446 The RF transmission systems were different between all the scanners used for data collection. This
447 is indeed a likely cause of variability of T1 and MTsat maps. Therefore, another obvious limitation
448 of this study is the lack of B1+ mapping. Unfortunately, a vendor-native B1+ mapping sequence
449 was not available on G1, and it is also well-known that discrepancies between vendor-native B1+

450 mapping contribute to between-scanner bias in T1 mapping³⁸. As for the VENUS protocol, the
451 current version of RTHawk did not permit the long gradient durations (e.g., 80ms) needed by AFI
452 implementation to achieve accurate B1+ mapping⁷⁰. Therefore, further investigation is needed to
453 compare vendor-neutral B1+ maps across vendors for isolating the specific contribution of
454 transmit field inhomogeneity.

455 Another critical factor affecting the accuracy is the calculation of a global RF scaling factor.
456 Vendor-native systems set the transmit gain using their own prescan routine, which may lead to a
457 systematic bias in quantitative mapping. In this work, we implemented prescan for G1 and S1-2
458 as described by¹³ and configured RTHawk to use the same calibration measurements.
459 Nevertheless, it is possible to make this step vendor-neutral as well. For future work, we plan to
460 develop a double-angle VENUS prescan using the same excitation pulses as the qMRI sequences
461 that follow, to determine a global RF scaling factor. Coupled with the use of anatomy-mimicking
462 quantitative MRI phantoms⁷¹, this would offer qMRI-ready adaptive prescan routines and help
463 investigate the effect of standardizing calibration measurements on multicenter accuracy and
464 agreement.

465 We made the details of the RTHawk reconstruction pipeline publicly available. However, the raw
466 data from the vendor-native acquisitions were not available. Open-source reconstruction tools⁵⁴⁻⁵⁶
467 are an important asset to investigate the potential effect of reconstruction pipeline differences on
468 image characteristics, such as the differences between resolution insert patterns observed in Fig.
469 3b-g. Therefore, future work will enable raw data export from vendor-native systems and add a
470 containerized reconstruction node to the qMRFLow⁵³ pipeline for investigating potential sources
471 of reconstruction variability.

472 Finally, the study of measurement stability using VENUS could benefit from recruiting more
473 participants and including more imaging sites. Although the inter-vendor pattern observed in our
474 limited cohort is consistent across 3 scanners, within-vendor (S1-vs-S2) results from vendor-native
475 implementations are more consistent and comparable to VENUS (Fig. 7). Nevertheless, more data
476 is needed for a thorough characterization of subject specific within-vendor effects. Our future
477 study will deploy VENUS on more GE and Siemens sites and recruit more participants to
478 investigate the variability problem from different perspectives, including system upgrades and
479 WM pathology.

480 **Conclusion**

481 In this article we have demonstrated that vendor-neutral sequences and transparent workflows
482 reduce inter-vendor variability in quantitative MRI. Additionally, these workflows can be
483 deployed on an FDA-approved device, which demonstrates the potential for wide clinical
484 adoption. Quantitative MRI needs to bypass the vendor black boxes to make an impact in the clinic,
485 and this work shows the way forward.

486

487 **Tables**

488 **Table 1** Comparison of acquisition parameters between vendor-native and vendor-neutral protocols. Parameters that
 489 are hardcoded on vendor-native systems are denoted by an asterisk (*).

	Common acquisition parameters			
FA (°) PDw/MTw/T1w	6/6/20			
MT PDw/MTw/T1w	off/on/off			
Voxel size (mm)	1x1x3			
TR (ms) PDw/MTw/T1w	32/32/18			
TE (ms)	4			
FOV (cm)	25.6			
Receiver bandwidth (kHz)	62.5			
MT frequency offset (Hz)*	1200			
Scanner ID and sequence type	G1_{NATIVE}	S1_{NATIVE}	S2_{NATIVE}	G1, S1-2_{VENUS}
Sequence name	3D SPGR	3D FLASH	3D FLASH	mt_sat (v1.1.0)
MT pulse shape*	Fermi	Gaussian	Gaussian	Fermi
MT pulse duration (ms)*	8	10	10	12
RF phase increment (°)*	115.4	50	50	117

490

491

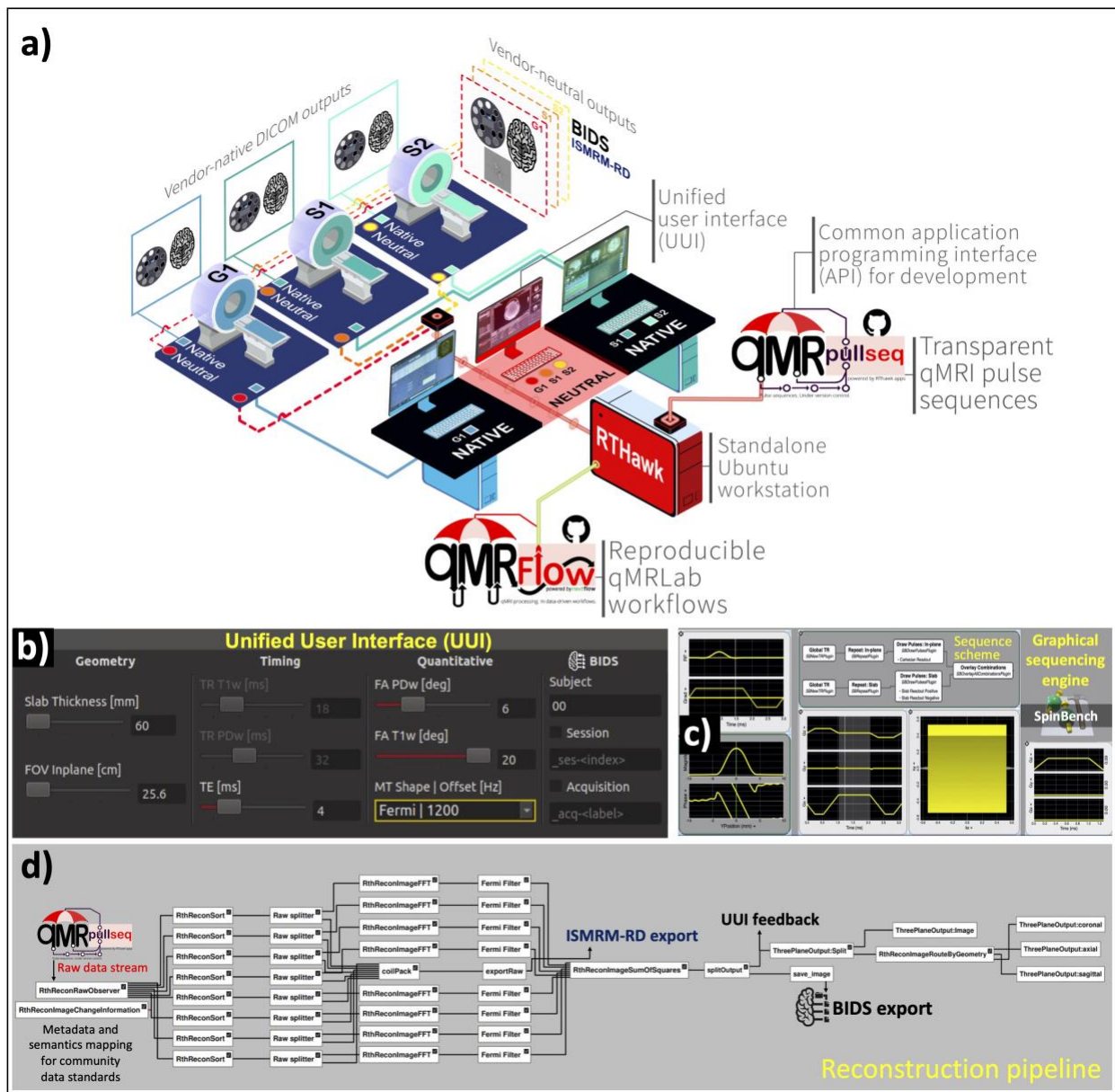
492
493
494

Table 2 Coefficient of variation (%) of vendor-neutral (VENUS) and vendor-native quantitative measurements between the scanners for each participant (P1-P3) and across participants.

Participants	P1		P2		P3		Across	
Protocol	NATIVE	VENUS	NATIVE	VENUS	NATIVE	VENUS	NATIVE	VENUS
T1	9.8	1.3	11.7	4.0	16.5	6.1	11.36	4.3
MTR	8.5	3.4	8.5	3.4	10.1	4.1	7.9	3.2
MTsat	13.6	5.9	11.9	3.4	12.1	4.1	10.7	4.2

495
496
497

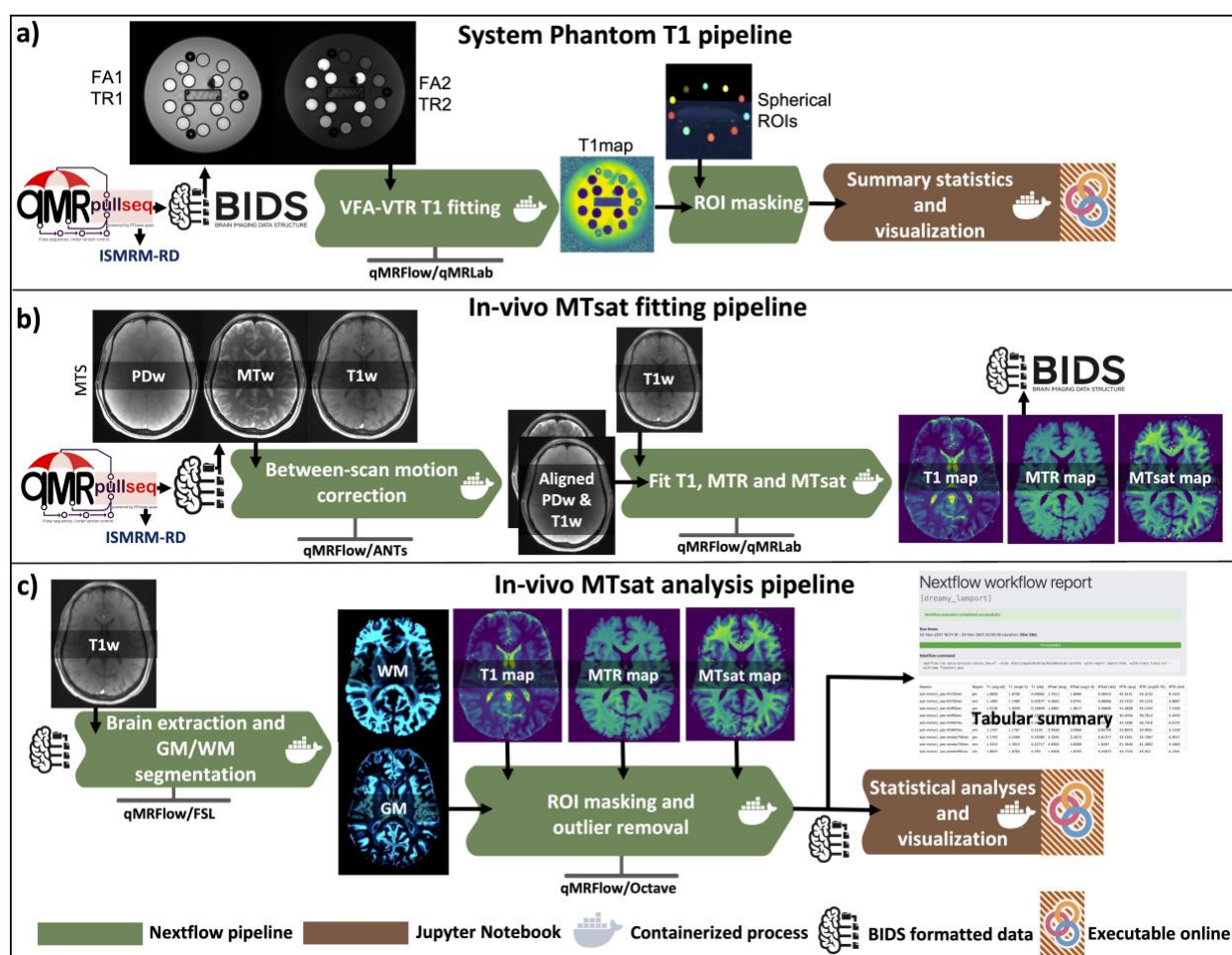
498 **Figures**



499

500 **Figure 1 - Schematic illustration of the experimental design for multicenter data collection**
 501 **using vendor-native and vendor-neutral pulse sequences and pulse sequence development**
 502 **components:** **a)** 3 MRI systems are located at 2 different sites and are labeled G1 (GE 750w), S1
 503 (Siemens Prisma) and S2 (Siemens Skyra). Vendor “Native” systems export data in the DICOM
 504 format. The proposed vendor-agnostic “Neutral” system can export a complete set of reconstructed
 505 images in BIDS and the k-space data in ISMRM-RD format, synchronized across MRI systems.
 506 Connecting to the MRI system(s) over the local network, RTHawk (red workstation) can play

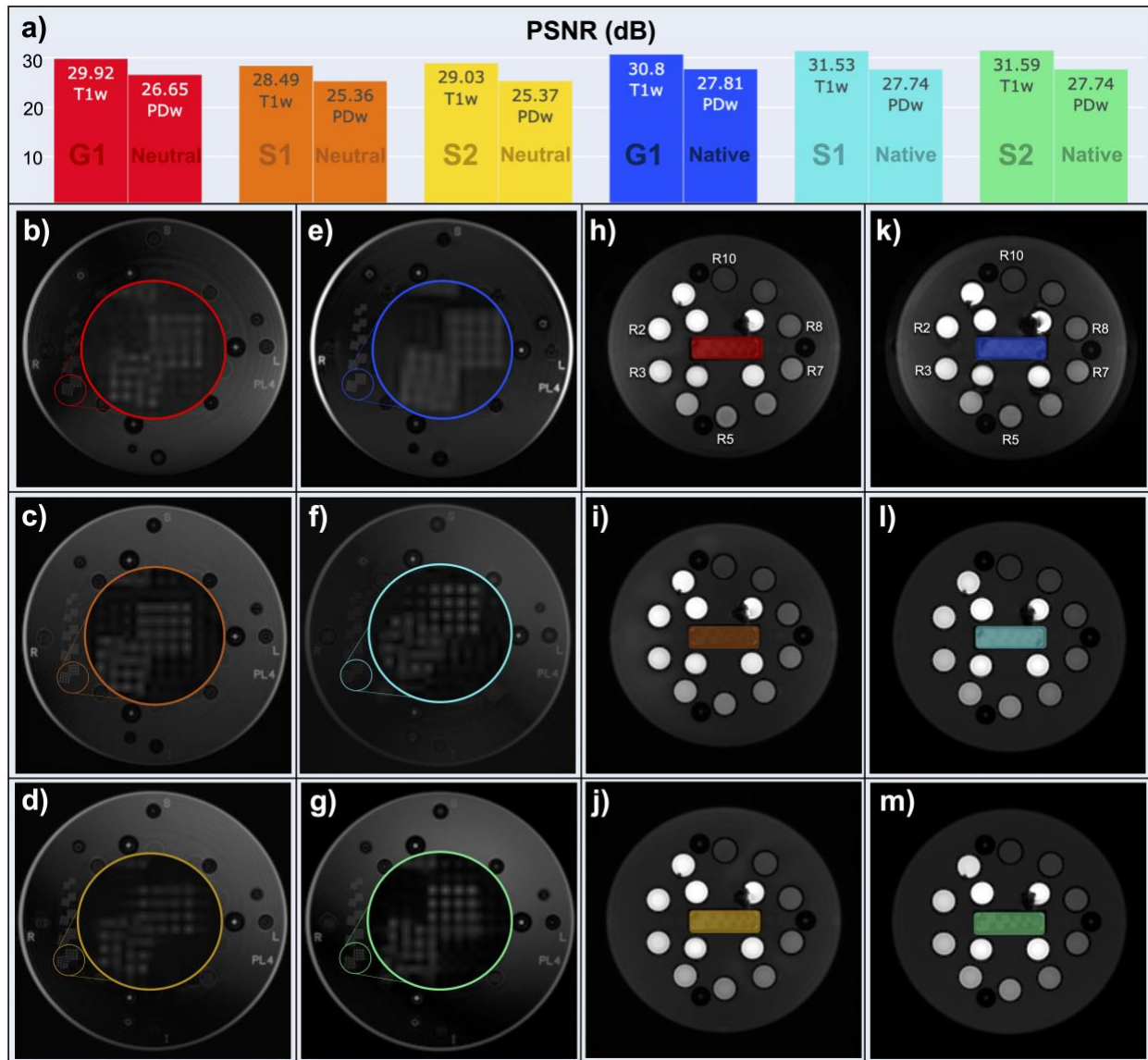
507 open-source qMRI pulse sequences under version control (qMRPullseq). All the sequences are
 508 publicly available at https://github.com/qmrlab/pulse_sequences. Fully containerized qMRFlow
 509 data-driven pipelines can connect to the scanner data stream for post-processing on the RTHawk
 510 workstation (red workstation). The same pipelines can be reproduced on a local computer,
 511 supercomputing clusters or in the cloud. **b)** The acquisitions are controlled using a unified user
 512 interface (UI), providing a consistent user experience across vendors. **c)** RF and gradient
 513 waveform stub blocks together with the readout logic are developed using SpinBench. **d)** RTHawk
 514 reconstruction pipeline nodes are illustrated for an 8-channel receiver, also indicating how raw and
 515 reconstructed data are exported and forwarded to the display tools for on-site visualization.



516

517 **Figure 2 – Image quality assessment using the phantom: a)** Peak SNR values (PSNR) from
 518 T1w and PDw phantom images are displayed for vendor-neutral (red, orange, and yellow) and
 519 vendor-native (blue, cyan, and teal) G1, S1 and S2 scans, respectively. The same color coding is

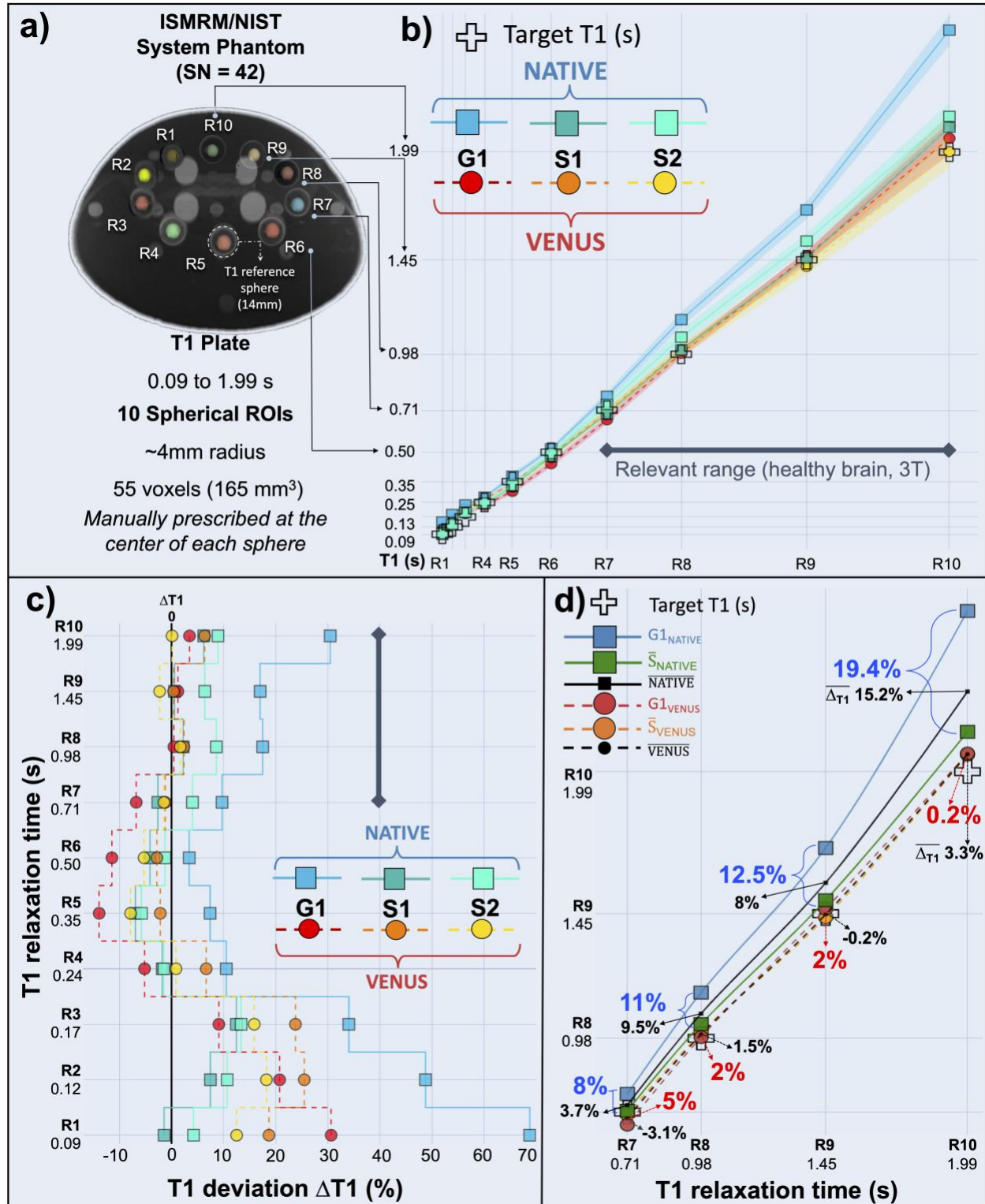
520 used in the following panels. **b-g)** Coronal PDw phantom images, with an inset zoom on two 4x4
 521 grids with 1mm spacing. The brightness of the zoomed-in insets is increased by 30% for display
 522 purposes. **h-m)** Coronal T1w phantom images showing the center of the reference T1 arrays. The
 523 fine resolution (<0.6mm) inserts located at the center of the T1 array (rectangular area) are not
 524 relevant for the present resolution level. These inserts are colored following the same convention
 525 described in a) for convenience.



526

527 **Figure 3 - Overview of the analysis workflow for phantom scans (a) and in vivo scans (b, c).**
 528 File collection (MTS) and output map names (T1map, MTsat, MTRmap) follow the BIDS standard
 529 v1.6.0. a) Vendor-neutral and vendor-native phantom images were acquired at two flip angles and

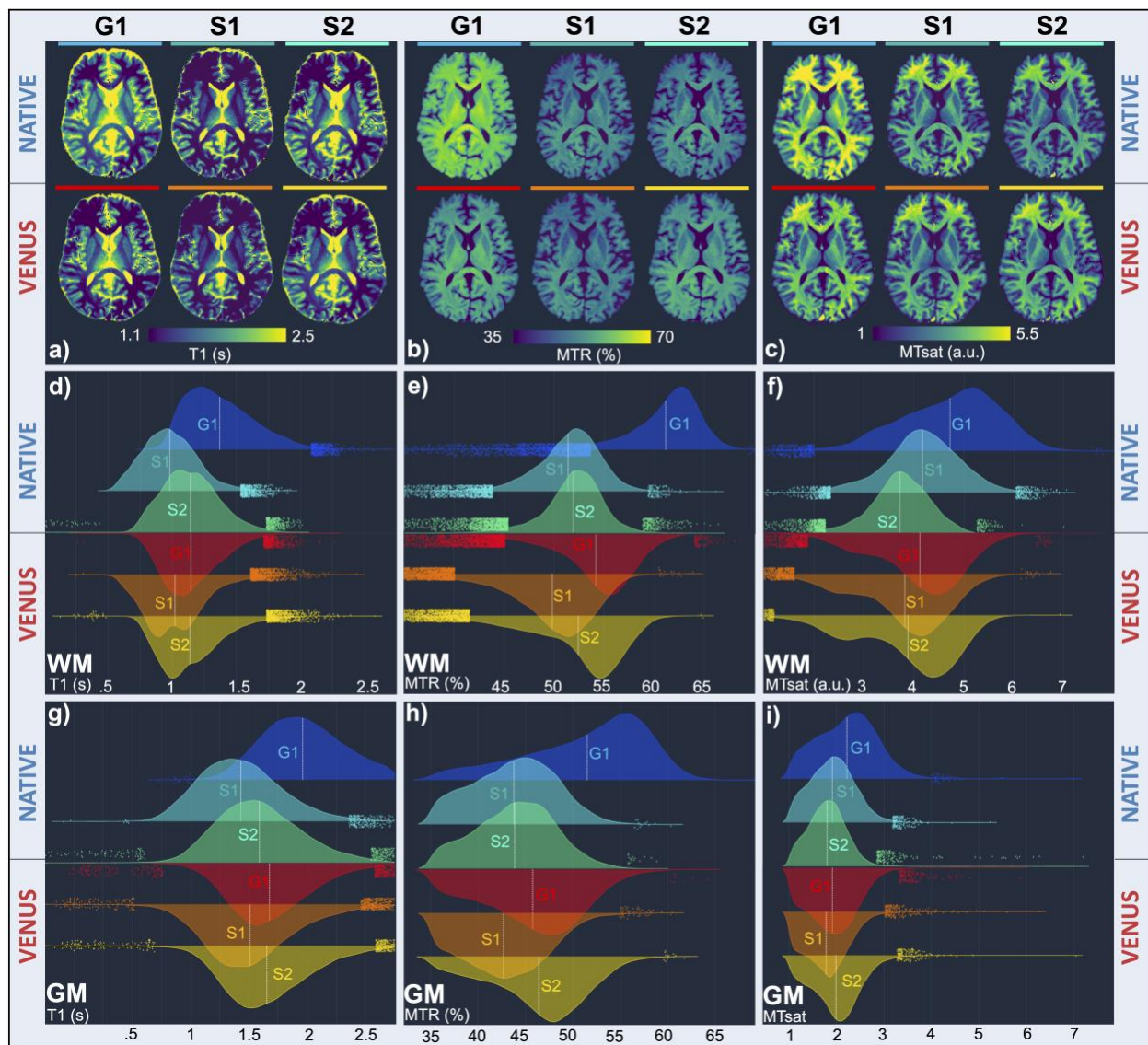
530 two repetition times. The output data are then subjected to T1 fitting using qMRLab (Docker
531 container image: qmrlab/minimal:v2.5.0b). The resulting T1 maps are masked using manually
532 prescribed 10 spherical ROIs (reference T1 ranging from 0.9 to 1.9s). **b)** PDw and MTw images
533 are aligned to the T1w image to correct for between-scan motion. The aligned dataset is then
534 subjected to MTsat and MTR fitting in qMRLab to generate T1map, MTRmap and MTsat. **c)** Brain
535 extraction and tissue type segmentation is performed on the T1w images using FSL. Following
536 region masking and outlier removal for each map, vector outputs are saved for statistical analysis
537 and visualization in an online-executable Jupyter Notebook (R-Studio and Python) environment.
538 The tabular summary and the Nextflow pipeline execution report are exported. The pipeline
539 execution report is available at <https://qmrlab.org/VENUS/qmrflow-exec-report.html>.



540

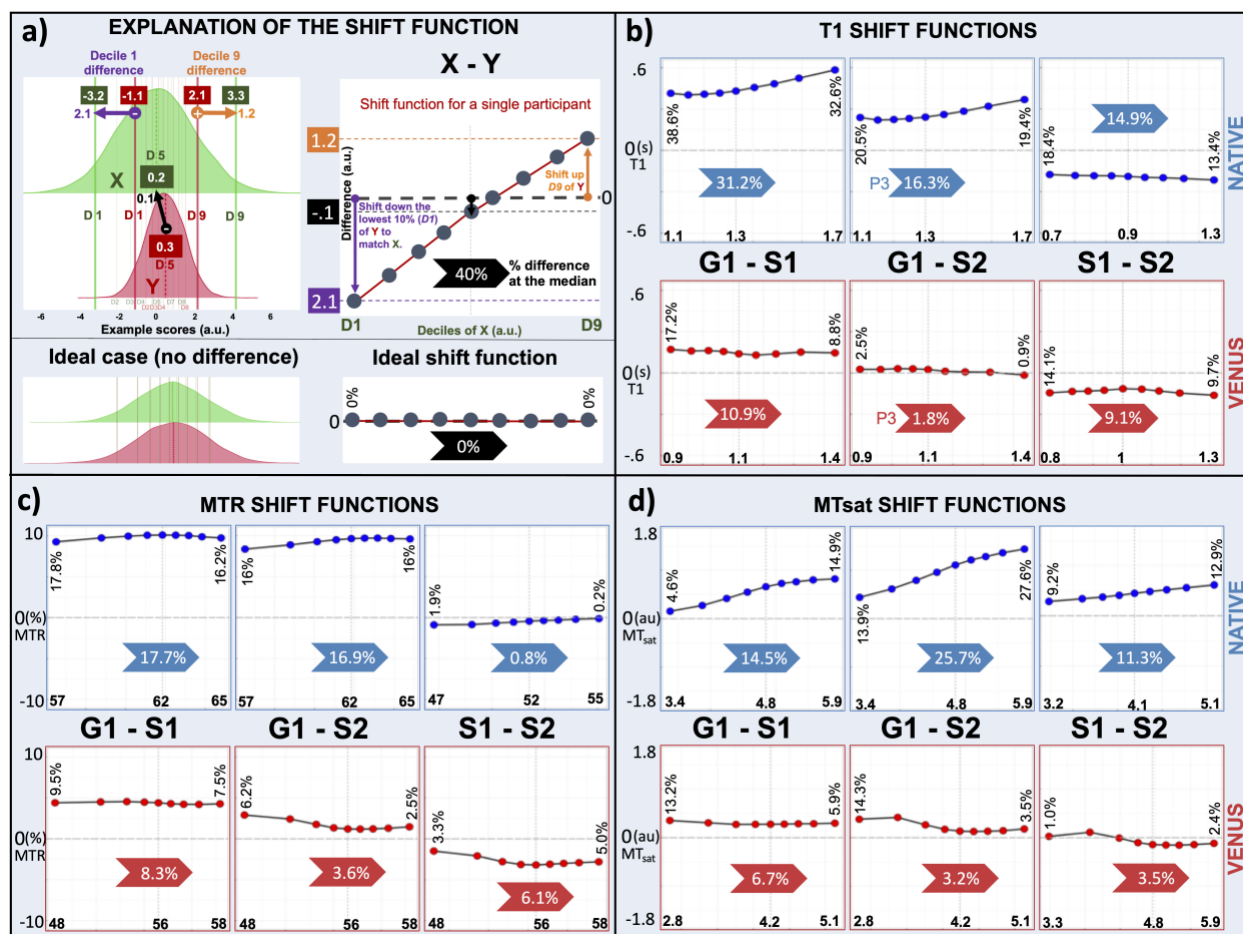
541 **Figure 4** - Comparison of vendor-native and vendor-neutral T1 measurements in the studied range
 542 of the phantom reference values, from 0.09 to 1.99s (a). T1 values from the vendor-native
 543 acquisitions are represented by solid lines and square markers in cold colors, and those from

544 VENUS attain dashed lines and circle markers in hot colors. **b)** Vendor-native measurements,
 545 especially $G1_{NATIVE}$ and $S2_{NATIVE}$, overestimate T1. $G1_{VENUS}$ and $S1-2_{VENUS}$ remain closer to the
 546 reference. **c)** For VENUS, $\Delta T1$ remains low for R7 to R10, whereas deviations reach up to 30.4%
 547 for vendor-native measurements. **d)** T1 values are averaged over S1-2 (\bar{S}_{NATIVE} and \bar{S}_{VENUS} , green
 548 square and orange circle) and according to the acquisition type (\bar{N}_{NATIVE} and \bar{V}_{VENUS} , black square
 549 and black circle). Inter-vendor percent differences are annotated in blue (native) and red (VENUS).
 550 Averaged percent measurement errors ($\overline{\Delta T1}$) are annotated on the plot (black arrows).



551
 552 **Figure 5- Vendor-native and VENUS quantitative maps** from one participant are shown in one
 553 axial slice (a-c). Distributions of quantified parameters in white matter (d-f) and gray matter (g-i)

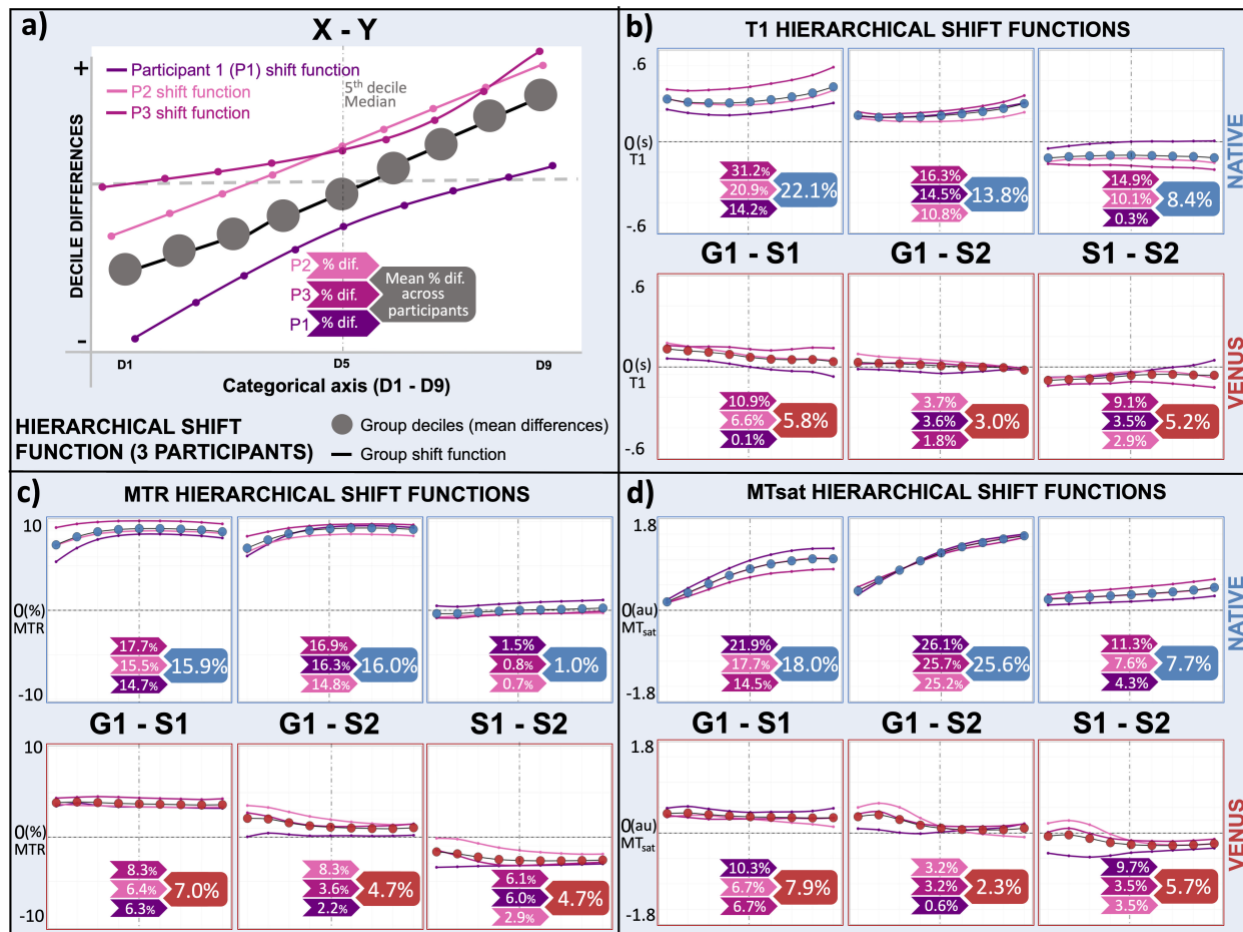
554 are shown using ridgeline plots of kernel density estimations. **a-c)** Inter-vendor images (G1 vs S1
 555 and G1 vs S2) appear more similar in VENUS (lower row) than in native (upper row). **d-f)**
 556 Distribution shapes and locations agree with visual inspection from (a), indicating closer
 557 agreement between VENUS distributions. **g-i)** Superior between-scanner agreement of VENUS
 558 persists in GM as well. Compared to WM, GM distributions are in the expected range (higher T1,
 559 lower MTR and MTsat values).



560

561 **Figure 6 - Shift function analysis of T1, MTR and MTsat results from a single participant in**
 562 **white-matter (WM).** **a)** Shift function analysis is a graphical tool for analyzing differences
 563 between two (dependent in this case) measurements at any location of the distributions. It shows
 564 9 markers dividing the distribution into 10 equal chunks; hence the markers represent deciles. The
 565 shape of the curve (shift function) obtained by plotting decile differences against the first decile
 566 characterizes how distributions differ from each other. **b-d)** Here, shift function plots compare the
 567 agreement between different scanners for VENUS (bottom row) and vendor-native (top row)

568 implementations in quantifying T1, MTR and MTsat. Across all the comparisons, the apparent
 569 trend is that the VENUS inter-vendor variability is lower than for the vendor-native
 570 implementations.



571
 572 **Figure 7 – Hierarchical shift function analysis of T1, MTR and MTsat results from three**
 573 **participants in the white-matter (WM).** **a)** Hierarchical shift function repeats Figure 6 for all
 574 participants (shades of pink). Group deciles (red and blue markers for VENUS and vendor-native,
 575 respectively) show the average trend of inter-scanner differences across participants. **b-d)** G1-vs-
 576 S1 and G1-vs-S2 (inter-vendor) agree in VENUS better than they do in vendor-native for all
 577 quantitative maps of T1, MTR and MTsat.

578 **Acknowledgement**

579 The authors would like to acknowledge Graham Wright, PhD for his help in organizing the
580 multicenter experiment, Paule Samson for her help in data collection, Juan Santos, PhD and
581 William R. Overall, PhD for their technical support in deploying RTHawk on multiple sites.

582 **Data availability statement**

583 All the vendor-neutral pulse sequences are publicly available as git submodules at
584 https://github.com/qmrlab/pulse_sequences and can be run on RTHawk systems v3.0.0 and later.
585 The RF and gradient waveforms (spv files) can be inspected and simulated using SpinBench
586 (<https://www.heartvista.ai/spinbench>). As per the general design principles of fully reproducible
587 qMRFlow pipelines, we adhered to a one-process one-container mapping for the processing of this
588 dataset. Docker images, BIDS and ISMRM-RD compliant dataset from the current study are freely
589 available at <https://doi.org/10.17605/osf.io/5n3cu>. Finally, the whole analysis and interactive
590 version of all the figures in this article will be available and executable online at
591 <https://github.com/qmrlab/venus>.

592 **References**

- 593 1. Lauterbur PC. Image formation by induced local interactions: examples employing nuclear
594 magnetic resonance. *nature*. 1973;242(5394):190-191. doi:10.1038/242190a0
- 595 2. Gillies RJ, Kinahan PE, Hricak H. Radiomics: Images Are More than Pictures, They Are Data.
596 *Radiology*. Feb 2016;278(2):563-77. doi:10.1148/radiol.2015151169
- 597 3. Novikov DS, Kiselev VG, Jespersen SN. On modeling. *Magn Reson Med*. Jun
598 2018;79(6):3172-3193. doi:10.1002/mrm.27101
- 599 4. Hahn EL. An Accurate Nuclear Magnetic Resonance Method for Measuring Spin-Lattice
600 Relaxation Times. *Phys Rev*. 1949;76(1):145-146. doi:10.1103/PhysRev.76.145
- 601 5. Gupta RK. A new look at the method of variable nutation angle for the measurement of
602 spin-lattice relaxation times using fourier transform NMR. *Journal of Magnetic Resonance*.
603 1977;25(1):231-235. doi:10.1016/0022-2364(77)90138-X
- 604 6. D.C. Look, Locker DR. Time saving in measurement of NMR and EPR relaxation times.
605 *Review of Scientific Instruments*. 1970;41(2):250-251. doi:10.1063/1.1684482
- 606 7. Marques JP, Kober T, Krueger G, van der Zwaag W, Van de Moortele PF, Gruetter R.
607 MP2RAGE, a self bias-field corrected sequence for improved segmentation and T1-mapping at
608 high field. *Neuroimage*. Jan 15 2010;49(2):1271-81. doi:10.1016/j.neuroimage.2009.10.002
- 609 8. Stikov N, Boudreau M, Levesque IR, Tardif CL, Barral JK, Pike GB. On the accuracy of T1
610 mapping: searching for common ground. *Magn Reson Med*. Feb 2015;73(2):514-22.
611 doi:10.1002/mrm.25135
- 612 9. Grafe D, Frahm J, Merckenschlager A, Voit D, Hirsch FW. Quantitative T1 mapping of the
613 normal brain from early infancy to adulthood. *Pediatr Radiol*. Mar 2021;51(3):450-456.
614 doi:10.1007/s00247-020-04842-7

- 615 10. Okubo G, Okada T, Yamamoto A, et al. MP2RAGE for deep gray matter measurement of
616 the brain: A comparative study with MPRAGE. *J Magn Reson Imaging*. Jan 2016;43(1):55-62.
617 doi:10.1002/jmri.24960
- 618 11. Voelker MN, Kraff O, Goerke S, et al. The traveling heads 2.0: Multicenter reproducibility
619 of quantitative imaging methods at 7 Tesla. *Neuroimage*. May 15 2021;232:117910.
620 doi:10.1016/j.neuroimage.2021.117910
- 621 12. Bane O, Hectors SJ, Wagner M, et al. Accuracy, repeatability, and interplatform
622 reproducibility of T1 quantification methods used for DCE-MRI: Results from a multicenter
623 phantom study. *Magnetic Resonance in Medicine*. 2018;79(5):2564-2575.
624 doi:10.1002/mrm.26903
- 625 13. Keenan KE, Gimbutas Z, Dienstfrey A, et al. Multi-site, multi-platform comparison of MRI
626 T1 measurement using the system phantom. *PLOS ONE*. 2021;16(6):e0252966.
627 doi:10.1371/journal.pone.0252966
- 628 14. Yarnykh VL. Optimal radiofrequency and gradient spoiling for improved accuracy of T1
629 and B1 measurements using fast steady-state techniques. *Magnetic Resonance in Medicine*.
630 2010;63(6):1610-1626. doi:10.1002/mrm.22394
- 631 15. A.G. Teixeira RP, Malik SJ, Hajnal JV. Fast quantitative MRI using controlled saturation
632 magnetization transfer. *Magnetic Resonance in Medicine*. 2019;81(2):907-920.
633 doi:10.1002/mrm.27442
- 634 16. Bojorquez JZ, Bricq S, Acquitter C, Brunotte F, Walker PM, Lalande A. What are normal
635 relaxation times of tissues at 3 T? *Magn Reson Imaging*. Jan 2017;35:69-80.
636 doi:10.1016/j.mri.2016.08.021
- 637 17. Cohen-Adad J, Alonso-Ortiz E, Abramovic M, et al. Open-access quantitative MRI data of
638 the spinal cord and reproducibility across participants, sites and manufacturers. *Sci Data*. Aug 16
639 2021;8(1):219. doi:10.1038/s41597-021-00941-8
- 640 18. Liberman G, Louzoun Y, Ben Bashat D. T(1) mapping using variable flip angle SPGR data
641 with flip angle correction. *J Magn Reson Imaging*. Jul 2014;40(1):171-80. doi:10.1002/jmri.24373
- 642 19. Leutritz T, Seif M, Helms G, et al. Multiparameter mapping of relaxation (R1, R2*), proton
643 density and magnetization transfer saturation at 3 T: A multicenter dual-vendor reproducibility
644 and repeatability study. *Hum Brain Mapp*. Oct 15 2020;41(15):4232-4247.
645 doi:10.1002/hbm.25122
- 646 20. Boudreau M, Stikov N, Pike GB. B1 -sensitivity analysis of quantitative magnetization
647 transfer imaging. *Magn Reson Med*. Jan 2018;79(1):276-285. doi:10.1002/mrm.26673
- 648 21. Gracien R-M, Maiworm M, Brüche N, et al. How stable is quantitative MRI? – Assessment
649 of intra- and inter-scanner-model reproducibility using identical acquisition sequences and data
650 analysis programs. *NeuroImage*. 2020;207:116364. doi:10.1016/j.neuroimage.2019.116364
- 651 22. Helms G, Dathe H, Dechent P. Quantitative FLASH MRI at 3T using a rational
652 approximation of the Ernst equation. *Magn Reson Med*. Mar 2008;59(3):667-72.
653 doi:10.1002/mrm.21542
- 654 23. Rowley CD, Campbell JSW, Wu Z, et al. A model-based framework for correcting B1 +
655 inhomogeneity effects in magnetization transfer saturation and inhomogeneous magnetization
656 transfer saturation maps. *Magn Reson Med*. Oct 2021;86(4):2192-2207. doi:10.1002/mrm.28831
- 657 24. Stikov N, Trzasko JD, Bernstein MA. Reproducibility and the future of MRI research. *Magn
658 Reson Med*. Dec 2019;82(6):1981-1983. doi:10.1002/mrm.27939

- 659 25. Jochimsen TH, Von Mengershausen M. ODIN—object-oriented development interface for
660 NMR. *Journal of Magnetic Resonance*. 2004;170(1):67-78. doi:10.1016/j.jmr.2004.05.021
- 661 26. Stöcker T, Vahedipour K, Pflugfelder D, Shah NJ. High-performance computing MRI
662 simulations. *Magnetic resonance in medicine*. 2010;64(1):186-193. doi:10.1002/mrm.22406
- 663 27. Magland JF, Li C, Langham MC, Wehrli FW. Pulse sequence programming in a dynamic
664 visual environment: SequenceTree. *Magnetic resonance in medicine*. 2016;75(1):257-265.
665 doi:10.1002/mrm.25640
- 666 28. Ravi KS, Geethanath S, Vaughan JT. PyPulseq: A python package for mri pulse sequence
667 design. *Journal of Open Source Software*. 2019;4(42):1725.
- 668 29. Layton KJ, Kroboth S, Jia F, et al. Pulseq: a rapid and hardware-independent pulse
669 sequence prototyping framework. *Magnetic resonance in medicine*. 2017;77(4):1544-1552.
670 doi:10.1002/mrm.26235
- 671 30. Nielsen JF, Noll DC. TOPPE: A framework for rapid prototyping of MR pulse sequences.
672 *Magnetic resonance in medicine*. 2018;79(6):3128-3134. doi: 10.1002/mrm.26990
- 673 31. Cordes C, Konstandin S, Porter D, Günther M. Portable and platform-independent MR
674 pulse sequence programs. *Magnetic resonance in medicine*. 2020;83(4):1277-1290.
675 doi:10.1002/mrm.28020
- 676 32. Zwart NR, Pipe JG. Graphical programming interface: A development environment for
677 MRI methods. *Magnetic resonance in medicine*. 2015;74(5):1449-1460. doi:10.1002/mrm.25528
- 678 33. Ravi KS, Potdar S, Poojar P, et al. Pulseq-Graphical Programming Interface: Open source
679 visual environment for prototyping pulse sequences and integrated magnetic resonance imaging
680 algorithm development. *Magnetic resonance imaging*. 2018;52:9-15. doi:10.21105/joss.01725
- 681 34. Herz K, Mueller S, Perlman O, et al. Pulseq-CEST: Towards multi-site multi-vendor
682 compatibility and reproducibility of CEST experiments using an open-source sequence standard.
683 *Magnetic resonance in medicine*. 2021;86(4):1845-1858. doi:10.1002/mrm.28825
- 684 35. Tong G, Gaspar AS, Qian E, et al. A framework for validating open-source pulse sequences.
685 *Magnetic resonance imaging*. 2021;87:7-18. doi:10.1016/j.mri.2021.11.014
- 686 36. Barral JK, Gudmundson E, Stikov N, Etezadi-Amoli M, Stoica P, Nishimura DG. A robust
687 methodology for in vivo T1 mapping. *Magn Reson Med*. Oct 2010;64(4):1057-67.
688 doi:10.1002/mrm.22497
- 689 37. Santos JM, Wright GA, Pauly JM. Flexible real-time magnetic resonance imaging
690 framework. In: *Conf Proc IEEE Eng Med Biol Soc*. 2004:1048-1051.
- 691 38. Lee Y, Callaghan MF, Acosta-Cabronero J, Lutti A, Nagy Z. Establishing intra- and inter-
692 vendor reproducibility of T1 relaxation time measurements with 3T MRI. *Magn Reson Med*. Jan
693 2019;81(1):454-465. doi:10.1002/mrm.27421
- 694 39. Leutritz T, Seif M, Helms G, et al. Multiparameter mapping of relaxation (R1, R2*), proton
695 density and magnetization transfer saturation at 3 T: A multicenter dual-vendor reproducibility
696 and repeatability study. *Human brain mapping*. 2020;41(15):4232-4247. doi:10.1002/hbm.25122
- 697 40. Helms G, Dathe H, Kallenberg K, Dechent P. High-resolution maps of magnetization
698 transfer with inherent correction for RF inhomogeneity and T1 relaxation obtained from 3D
699 FLASH MRI. *Magn Reson Med*. Dec 2008;60(6):1396-407. doi:10.1002/mrm.21732
- 700 41. Haase A, Frahm J, Matthaei D, Hänicke W, Merboldt KD. FLASH imaging: rapid NMR
701 imaging using low flip-angle pulses. 1986. *J Magn Reson*. Dec 2011;213(2):533-41.
702 doi:10.1016/j.jmr.2011.09.021

- 703 42. Inati SJ, Naegele JD, Zwart NR, et al. ISMRM Raw data format: A proposed standard for
704 MRI raw datasets. *Magnetic resonance in medicine*. 2017;77(1):411-421.
705 doi:10.1002/mrm.26089
- 706 43. Gorgolewski KJ, Auer T, Calhoun VD, et al. The brain imaging data structure, a format for
707 organizing and describing outputs of neuroimaging experiments. *Scientific data*. 2016;3(1):1-9.
708 doi:10.1038/sdata.2016.44
- 709 44. Karakuzu A, Appelhoff S, Auer T, et al. qMRI-BIDS: an extension to the brain imaging data
710 structure for quantitative magnetic resonance imaging data. *medRxiv*.
711 2021:2021.10.22.21265382. doi:10.1101/2021.10.22.21265382
- 712 45. Cohen-Adad J, Alonso-Ortiz E, Abramovic M, et al. Generic acquisition protocol for
713 quantitative MRI of the spinal cord. *Nature protocols*. 2021;16(10):4611-4632.
714 doi:10.1038/s41596-021-00588-0
- 715 46. Karakuzu A, Boudreau M, Duval T, et al. qMRLab: Quantitative MRI analysis, under one
716 umbrella. *Journal of Open Source Software*. 2020;5(53):2343. doi:10.21105/joss.02343
- 717 47. Avants BB, Tustison NJ, Song G, Cook PA, Klein A, Gee JC. A reproducible evaluation of
718 ANTs similarity metric performance in brain image registration. *Neuroimage*. 2011;54(3):2033-
719 2044. doi:10.1016/j.neuroimage.2010.09.025
- 720 48. Jenkinson M, Beckmann CF, Behrens TEJ, Woolrich MW, Smith SM. FSL. *Neuroimage*.
721 2012;62(2):782-790. doi:10.1016/j.neuroimage.2011.09.015
- 722 49. Keenan KE, Gimbutas Z, Dienstfrey A, Stupic KF. Assessing effects of scanner upgrades for
723 clinical studies. *Journal of Magnetic Resonance Imaging*. 2019;50(6):1948-1954.
724 doi:10.1002/jmri.26785
- 725 50. Rousselet GA, Pernet CR, Wilcox RR. Beyond differences in means: robust graphical
726 methods to compare two groups in neuroscience. *European Journal of Neuroscience*.
727 2017;46(2):1738-1748. doi:10.1111/ejn.13610
- 728 51. Harrell FE, Davis CE. A new distribution-free quantile estimator. *Biometrika*.
729 1982;69(3):635-640. doi:10.2307/2335999
- 730 52. Karakuzu A, Boudreau M, Cohen-Adad J, Stikov N. Thinking outside the blackbox: A fully
731 transparent T1 mapping pipeline. In: *Proc. Intl. Soc. Mag. Reson. Med. 28 (2020)*. 2020:4791.
- 732 53. Karakuzu A, Boudreau M, Duval T, et al. The qMRLab workflow: From acquisition to
733 publication. In: *Proc. Intl. Soc. Mag. Reson. Med. 27 (2019)*. 2019:4832.
- 734 54. Hansen MS, Sørensen TS. Gadgetron: an open source framework for medical image
735 reconstruction. *Magnetic resonance in medicine*. 2013;69(6):1768-1776.
736 doi:10.1002/mrm.24389
- 737 55. Assländer J, Cloos MA, Knoll F, Sodickson DK, Hennig J, Lattanzi R. Low rank alternating
738 direction method of multipliers reconstruction for MR fingerprinting. *Magnetic resonance in*
739 *medicine*. 2018;79(1):83-96. doi:10.1002/mrm.26639
- 740 56. Knopp T, Grosser M. MRIReco. jl: An MRI reconstruction framework written in Julia.
741 *Magnetic Resonance in Medicine*. 2021;86(3):1633-1646. doi:10.1002/mrm.28792
- 742 57. Maier O, Baete SH, Fyrdahl A, et al. CG-SENSE revisited: Results from the first ISMRM
743 reproducibility challenge. *Magnetic resonance in medicine*. 2021;85(4):1821-1839.
744 doi:10.1002/mrm.28569

- 745 58. Preibisch C, Deichmann R. Influence of RF spoiling on the stability and accuracy of T1
746 mapping based on spoiled FLASH with varying flip angles. *Magnetic Resonance in Medicine*.
747 2009;61(1):125-135. doi:10.1002/mrm.21776
- 748 59. Heule R, Ganter C, Bieri O. Variable flip angle T1 mapping in the human brain with reduced
749 t2 sensitivity using fast radiofrequency-spoiled gradient echo imaging. *Magnetic Resonance in*
750 *Medicine*. 2016;75(4):1413-1422. doi:10.1002/mrm.25668
- 751 60. Ashton E. Quantitative MR in multi-center clinical trials. *Journal of Magnetic Resonance*
752 *Imaging*. 2010;31(2):279-288. doi:10.1002/jmri.22022
- 753 61. Mancini M, Karakuzu A, Cohen-Adad J, Cercignani M, Nichols TE, Stikov N. An interactive
754 meta-analysis of MRI biomarkers of myelin. *eLife*. 2020;9doi:10.7554/elife.61523
- 755 62. Lazari A, Lipp I. Can MRI measure myelin? Systematic review, qualitative assessment, and
756 meta-analysis of studies validating microstructural imaging with myelin histology. *Neuroimage*.
757 2021;117744. doi:10.1016/j.neuroimage.2021.117744
- 758 63. Boshkovski T, Kocarev L, Cohen-Adad J, et al. The R1-weighted connectome:
759 complementing brain networks with a myelin-sensitive measure. *Network Neuroscience*.
760 2021;5(2):358-372. doi:10.1162/netn_a_00179
- 761 64. Badji A, de la Colina AN, Boshkovski T, et al. A Cross-Sectional Study on the Impact of
762 Arterial Stiffness on the Corpus Callosum, a Key White Matter Tract Implicated in Alzheimer's
763 Disease. *Journal of Alzheimer's Disease*. 2020;77:591-605. doi:10.3233/JAD-200668
- 764 65. Badji A, Noriega de la Colina A, Karakuzu A, et al. Arterial stiffness cut-off value and white
765 matter integrity in the elderly. *NeuroImage: Clinical*. 2020/01/01/ 2020;26:102007.
766 doi:10.1016/j.nicl.2019.102007
- 767 66. Weiskopf N, Edwards LJ, Helms G, Mohammadi S, Kirilina E. Quantitative magnetic
768 resonance imaging of brain anatomy and in vivo histology. *Nature Reviews Physics*. 2021/08/01
769 2021;3(8):570-588. doi:10.1038/s42254-021-00326-1
- 770 67. Salah K, Rehman MHU, Nizamuddin N, Al-Fuqaha A. Blockchain for AI: Review and Open
771 Research Challenges. *IEEE Access*. 2019;7:10127-10149. doi:10.1109/ACCESS.2018.2890507
- 772 68. Moritz M, Redlich T, Günay S, Winter L, Wulfsberg JP. On the economic value of open
773 source hardware—case study of an open source magnetic resonance imaging scanner. *Journal of*
774 *Open Hardware*. 2019;3(1):2. doi:10.5334/joh.14
- 775 69. DuPre E, Holdgraf C, Karakuzu A, et al. Beyond advertising: New infrastructures for
776 publishing integrated research objects. *PLOS Computational Biology*. 2022;18(1):e1009651.
777 doi:10.1371/journal.pcbi.1009651
- 778 70. Yarnykh VL. Actual flip-angle imaging in the pulsed steady state: A method for rapid three-
779 dimensional mapping of the transmitted radiofrequency field. *Magnetic Resonance in Medicine*.
780 2007;57(1):192-200. doi:10.1002/mrm.21120
- 781 71. Gopalan K, Tamir JI, Arias AC, Lustig M. Quantitative anatomy mimicking slice phantoms.
782 *Magnetic Resonance in Medicine*. 2021;86(2):1159-1166. doi:10.1002/mrm.28740
- 783
- 784